CrystEngComm

PAPER

View Article Online
View Journal | View Issue

Cite this: *CrystEngComm*, 2025, **27**, 5841

Stepwise assembly of Ni–N_2S_2 catalytic sites and porphyrin photosensitizers in a metal–organic framework for bioinspired photocatalysis†

Yu-Hao Gu, ‡ Xinyu Xu, ‡ Chenyu Zhu, Rengan Luo and Shuai Yuan *

Integrating biomimetic catalytic centers and photosensitizers into stable metal–organic frameworks (MOFs) holds great promise for efficient artificial photocatalysis. However, the direct incorporation of catalytic centers and photosensitizers are often hindered by the decomposition of biomimetic catalytic motifs under harsh solvothermal conditions typically required for synthesizing robust MOFs. In this work, we report a stepwise assembly strategy to incorporate biomimetic Ni–N_2S_2 catalytic sites and porphyrin-based photosensitizers into a stable Zr-based MOF for efficient photocatalysis. First, a Zr-MOF (Zr-NiTSC) bearing Ni-thiosemicarbazide (NiTSC) linkers was synthesized under mild conditions, preserving the structural integrity of the Ni–N_2S_2 sites. Subsequently, porphyrin-based linkers (DCPP) as photosensitizers were introduced *via* post-synthetic linker exchange, yielding a series of mixed-linker MOFs (Zr-NiTSC-P*x*, *x* = 1, 2, or 3). By fine-tuning the DCPP/NiTSC ratios, photocatalytic hydrogen evolution experiments revealed a non-monotonic dependence of photocatalytic hydrogen evolution activity on the DCPP/NiTSC ratio, with both insufficient and excessive photosensitizer content diminishing the activity. Zr-NiTSC-P2 achieved a balanced photosensitizer-to-catalyst ratio and the highest activity, with a 2.5-fold increase in turnover frequency compared to the parent MOF. This work demonstrates a stepwise synthetic strategy to integrate labile catalytic motifs into robust frameworks, offering a broadly applicable platform for constructing advanced photosensitized catalytic systems.

Received 21st June 2025,
Accepted 24th July 2025

DOI: 10.1039/d5ce00634a

rsc.li/crystengcomm

1. Introduction

Natural photosynthetic systems achieve efficient solar-to-chemical energy conversion through the spatial integration of light-harvesting photosensitizers and catalytic centers. For example, photoexcitation of chlorophylls in photosystem II drive water oxidation at a Mn_4CaO_5 cluster *via* tyrosine-mediated hole transfer,[1] achieving efficient solar energy conversion through the synergistic cooperation of light-harvesting photosensitizers and catalytic sites. Inspired by natural systems, biomimetic photocatalysis has emerged as a promising strategy for sustainable energy conversion.[2] Metal–organic frameworks (MOFs), with their high porosity, structural tunability, and functional modularity, provide an ideal platform for constructing biomimetic photocatalytic systems.[3] In particular, multivariate MOFs (MTV-MOFs) enable the co-integration of functionally distinct components (*e.g.*, catalytic sites and photosensitizers) within a crystalline lattice.[4] For example, Pt-based hydrogen evolution catalysts and Ir photosensitizers were integrated into a UiO-type MOF, resulting in stable photocatalytic H_2 evolution from water.[5] Recently, our group demonstrated that stable Zr-MOFs can serve as versatile platforms for tuning the stoichiometry between catalytic and photosensitizing units, unlocking new synergies in photocatalytic CO_2 reduction.[6]

Ni–N_2S_2 motifs replicate the active sites of [NiFe]-hydrogenases,[7] with molecular Ni–N_2S_2 catalysts demonstrating exceptional activity in the electrocatalytic hydrogen evolution reaction (HER).[8,9] Duan and co-workers employed Ni–N_2S_2 sites as nodes of a supramolecular cage, Ni-TFT, which efficiently catalyzed the photocatalytic HER combined with sulfide oxidation.[10] Recently, inspired by [NiFe]-hydrogenases, Jiang and co-workers achieved remarkable photocatalytic HER performance by anchoring Ni sites with N,O- or N,S-bidentate ligands on bipyridine units in a UiO-67-analogue framework, precisely tuning the primary and secondary coordination spheres.[11] Integrating Ni–N_2S_2 catalytic sites and photosensitizers within a stable MOF is expected to establish close spatial alignment between light-harvesting and catalytic functions, enabling efficient photoinduced charge separation and electron transfer

State Key Laboratory of Coordination Chemistry, School of Chemistry and Chemical Engineering, Nanjing University, Nanjing 210023, P. R. China. E-mail: syuan@nju.edu.cn

† Electronic supplementary information (ESI) available. CCDC 2419402. For ESI and crystallographic data in CIF or other electronic format see DOI: **https://doi.org/10.1039/d5ce00634a**

‡ These authors contributed equally to this work.

for high-performance photocatalysis. However, to our knowledge, the simultaneous integration of Ni–N_2S_2 catalytic sites and photosensitizers has not been achieved within a single framework. This is largely due to the intrinsic lability of Ni–N_2S_2 motifs, which readily decompose under the harsh solvothermal conditions typically used to synthesize robust MOFs. For instance, constructing stable Zr-based MOFs often requires high temperatures (~120 °C) and excess acid modulators. To overcome this limitation, we previously developed a stepwise strategy to synthesize stable Zr-MOFs under mild conditions: dynamic-bonded-based MOFs were initially synthesized as templates, followed by post-synthetic linker exchange with robust linkers to form stable Zr-MOFs.[12,13] This method provides new opportunities for the integration of Ni–N_2S_2 catalytic sites and photosensitizers into a Zr-based MOF, achieving stability and catalytic activity within a MOF scaffold.

Herein, we report a stepwise synthetic strategy for a dual-functional MOF photocatalyst that integrates catalytic hydrogen evolution sites and photosensitizers (Fig. 1). We designed a Ni-thiosemicarbazide-based dicarboxylate linker (NiTSC) with the Ni–N_2S_2 moiety as catalytically active sites (Fig. 1a). Meanwhile, we chose the length-matched dicarboxyphenyl porphyrin (DCPP) as the photosensitizer. The traditional one-pot reaction of Zr^{4+}, NiTSC and DCPP fails to form the mixed-linker Zr-MOF due to the decomposition of NiTSC at 120 °C, while the one-pot reaction at a lower temperature (75 °C) results in amorphous products (Fig. 1b). Additionally, the reaction between DCPP and Zr^{4+} under 120 °C tends to form interpenetrated frameworks, limiting the post-synthetic incorporation of the NiTSC linker.[14] In contrast, the assembly of Zr^{4+}, Ni^{2+}, and 4-[(2-carbamothioylhydrazineylidene)methyl]benzoic acid (TSC-COOH) linkers at 75 °C enables the formation of non-interpenetrated Zr-NiTSC (Fig. 1c). Subsequently, DCPP linkers are introduced *via* post-synthetic linker exchange, yielding a series of mixed-linker MOFs (Zr-NiTSC-P*x*; x = 1, 2, or 3) with tunable components. Photocatalytic HER studies revealed optimal activity at balanced linker ratios (Zr-NiTSC-P2, DCPP/NiTSC ≈ 1.3 : 1), achieving a 2.5-fold increase in the TOF compared to the pristine Zr-NiTSC.

2. Experimental section

2.1 Synthesis of linkers

Synthesis of TSC-COOH. The linker 4-((2-carbamothioylhydrazineylidene)methyl)benzoic acid (TSC-COOH) was synthesized through a Schiff-base reaction (Scheme S1†). Thiosemicarbazide (TSC, 2.28 g, 25 mmol) and *p*-formylbenzoic acid (PFBA, 3.75 g, 25 mmol) were dispersed in MeOH (150 mL) and heated to reflux for 3 hours. A light yellow solid TSC-COOH was collected through filtration, washed with MeOH, and dried under vacuum. ^{1}H NMR (400 MHz, DMSO): δ 13.06 (s, 1H), 11.58 (s, 1H), 8.31 (s, 1H), 8.11 (d, J = 11.5 Hz, 2H), 8.03–7.79 (m, 4H) (Fig. S1†).

Synthesis of single crystals of the NiTSC linker. To help determine the structure of MOFs, single crystals of the NiTSC linker were synthesized following the literature with modification (Scheme S2†).[15] A mixture of $NiCl_2{\cdot}6H_2O$ (12 mg, 0.05 mmol), TSC-COOH (22.3 mg, 0.1 mmol), Et_3N (100 μL), and MeCN (10 mL) was heated at 60 °C for 4 hours. After cooling down to room temperature, brown crystals were found at the bottom of the flask. The chemical formula of the obtained crystals of the NiTSC linker was determined to be $[NHEt_3]_2[Ni(TSC\text{-}COO)_2]{\cdot}2MeCN$ (CCDC 2419402, Fig. S2, and Table S1†).

Synthesis of H_2DCPP. 5,15-Di(4-carboxyphenyl)porphyrin (H_2DCPP) was synthesized according to the literature with modifications.[16] See the ESI† for details (Scheme S3 and Fig. S3 and S4). Fig. S5† compares the lengths of the NiTSC and DCPP linkers.

2.2 Synthesis of MOFs

Synthesis of Zr-NiTSC. $ZrOCl_2{\cdot}8H_2O$ (32 mg, 0.1 mmol), $Ni(OAc)_2{\cdot}4H_2O$ (50 mg, 0.2 mmol), TSC-COOH (180 mg, 0.8 mmol), acetic acid (AA, 100 μL), and *N*,*N*-dimethylacetamide

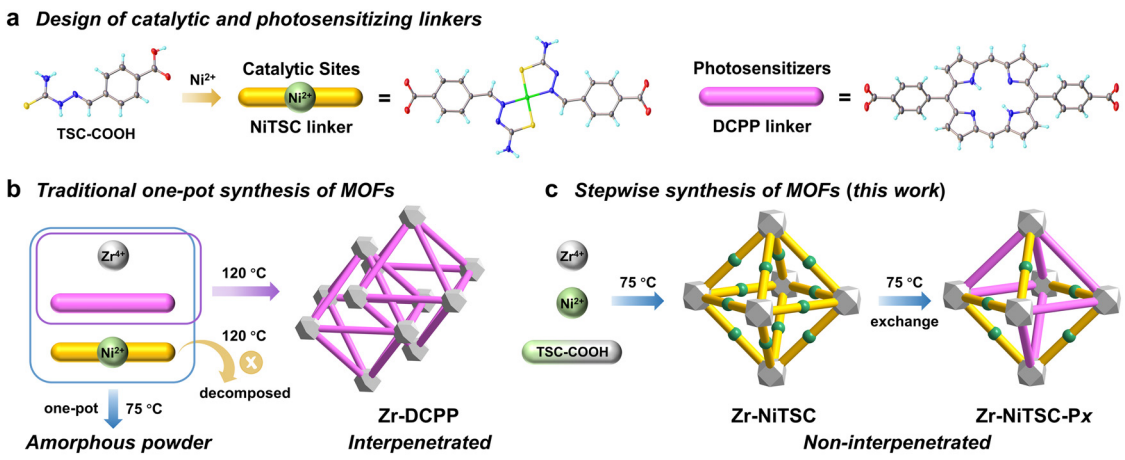

Fig. 1 (a) Design and single-crystal structures of NiTSC and DCPP linkers (green: Ni; yellow: S; blue: N; gray: C; red: O; light blue: H). Schematic diagram of the (b) traditional one-pot synthesis and (c) stepwise synthesis of Zr-NiTSC-P*x* (P stands for porphyrin, x = 1, 2, or 3).

(DMA, 10 mL) were charged in a glass tube and heated in a 75 °C oven for 3 days. The product Zr-NiTSC was collected by centrifugation and washed with *N*,*N*-dimethylformamide (DMF) and EtOH three times.

Synthesis of Zr-NiTSC-P*x* (*x* = 1, 2, or 3). Zr-NiTSC-P*x* was synthesized by post-synthetic linker exchange of Zr-NiTSC. Zr-NiTSC (10 mg) and different amounts of H_2DCPP were dispersed in 2 mL of DMF and heated in a 75 °C oven for 1 day. The products were collected by centrifugation and washed with DMF and EtOH three times. When 2 mg, 6 mg, or 10 mg of H_2DCPP was added, the products were denoted as Zr-NiTSC-P1, Zr-NiTSC-P2, or Zr-NiTSC-P3, respectively.

2.3 Photocatalytic H_2 evolution reactions

The photocatalytic HER experiments were performed with a photocatalytic evaluation system in a 170 mL quartz container. A 300 W xenon lamp was utilized as the irradiation source with an optical filter (cut 400 nm). The catalysts (5 mg) were dispersed in a MeCN/Et_3N solution (9 : 1 by vol, 30 mL), and H_2O (0.5 mL) was added. After sealing, the headspace of the container was purged with Ar (99.999%) for 30 min to remove air. During the 6 hours of reaction, the reaction system was stirred continuously with a magnetic bar to ensure that the catalysts were uniformly dispersed in the solution, and it was maintained at 25 °C by a circulating cooling water system. The H_2 production in the headspace of the reactor was measured using gas chromatography (GC).

3. Results and discussion

3.1 Design and synthesis of linkers incorporating Ni–N_2S_2 sites

To construct stable MOFs bearing Ni–N_2S_2 catalytic sites, we first rationally designed the linkers. The d^8 electronic configuration of Ni^{2+} favors the formation of square–planar complexes, and previous studies have reported various Ni–N_2S_2 planar complexes derived from TSC molecules and their derivatives, with the simplest examples being $Ni(TSC)_2(NO_3)_2$ and its deprotonated form $Ni(TSCATO)_2$.[17,18] Among the three nitrogen atoms in the TSC molecule, two are directly bonded to the C=S double bond. The conjugation effect and strong electron-withdrawing nature of the C=S bond significantly reduce the nucleophilicity of these two nitrogen atoms. In contrast, the terminal amino nitrogen atom retains strong nucleophilicity, readily forming imines *via* Schiff base reactions, thereby conferring excellent versatility to the Ni–N_2S_2 moiety. Reacting TSC molecules with various aldehyde-containing compounds yields diverse ligands, enabling the synthesis of imine complexes derived from the $Ni(TSC)_2$ unit with preserved Ni–N_2S_2 coordination.[19–22]

When designing suitable MOF linkers, the coordination geometry of the Ni–N_2S_2 center requires careful consideration. The planar Ni–N_2S_2 unit exhibits *cis* and *trans* isomers, with the *trans* configuration enabling two-connected linear linkers. Due to steric effects, the *trans*-Ni–N_2S_2 isomer is energetically favored and more readily formed.[17–22] The *cis* configuration is only accessible when the two nitrogen atoms are rigidly constrained by the molecular architecture.[23–25] This understanding guided our design of a linear linker based on *trans*-Ni–N_2S_2. We selected the simple *p*-formylbenzoic acid (PFBA), which underwent a Schiff base reaction with TSC to yield the TSC-COOH ligand (Scheme S1†). This afforded a linear Ni–N_2S_2 linker bearing terminal carboxyl groups at both ends (denoted as the NiTSC linker).

To confirm the structure of the NiTSC linker, single crystals of the ligand were successfully obtained for single-crystal X-ray diffraction (SCXRD) characterization. The reaction of Ni^{2+} with TSC-COOH in MeCN with a small amount of Et_3N gave dark brown crystals, which were suitable for diffraction (Scheme S2†). SCXRD analysis revealed that the asymmetric unit contains one deprotonated NiTSC linker, two protonated triethylamine molecules, and two MeCN solvent molecules, formulated as $[NHEt_3]_2[Ni(TSC\text{-}COO)_2]\cdot 2MeCN$ (Fig. S2† shows the full asymmetric unit, and Fig. 1a omits the counteranions and solvents for clarity). The carboxylate oxygen atoms participate in an extensive hydrogen-bonding network with amino groups from adjacent TSC fragments and protonated triethylamine molecules. The Ni–N_2S_2 center is electrically neutral, with the central nitrogen atom of the TSC fragment existing in a deprotonated state similar to that in $Ni(TSCATO)_2$,[18] resulting in a rigorously planar conjugated structure consistent with the anticipated *trans*-Ni–N_2S_2 configuration. The coplanarity of the phenyl ring with the Ni–N_2S_2 plane further corroborates the deprotonated state of the TSC fragment, since the non-deprotonated N–H bond would not allow such a coplanar configuration through steric hindrance with the phenyl C–H bond. This structural analysis unequivocally confirms that Ni^{2+} coordinates with TSC-COOH to form a linear, dicarboxylate-terminated linker, validating its suitability for subsequent MOF synthesis.

3.2 Design, synthesis, and structural analysis of Zr-NiTSC

According to the hard–soft acid–base (HSAB) theory, Ni^{2+} (a soft acid) tends to coordinate with N and S (soft base) to form Ni–N_2S_2 centers, whereas Zr^{4+} (a hard acid) preferentially binds to O (hard base) to form $Zr_6O_8(COO)_{12}$ clusters.[26] The previous literature has demonstrated that one-pot reactions can successfully assemble ordered multicomponent MOFs featuring simultaneous hard acid–hard base and soft acid–soft base coordination bonds.[12,27] Thus, in a one-pot reaction involving Zr^{4+}, Ni^{2+}, and TSC-COOH, we could predict the assembly of Zr-MOFs incorporating the NiTSC carboxylate linker. We conducted the reaction of $ZrOCl_2\cdot 8H_2O$, $Ni(OAc)_2\cdot 4H_2O$, and TSC-COOH at 75 °C, which yielded the brown powder of Zr-NiTSC. Powder X-ray diffraction (PXRD) analysis confirmed the high crystallinity of Zr-NiTSC (Fig. S6†). The peak profile closely resembles that of the UiO-series,[28] suggesting a framework structure based on Zr_6 clusters and ditopic linkers with the **fcu** topology. The structure of Zr-NiTSC (Fig. 2a) was further confirmed by

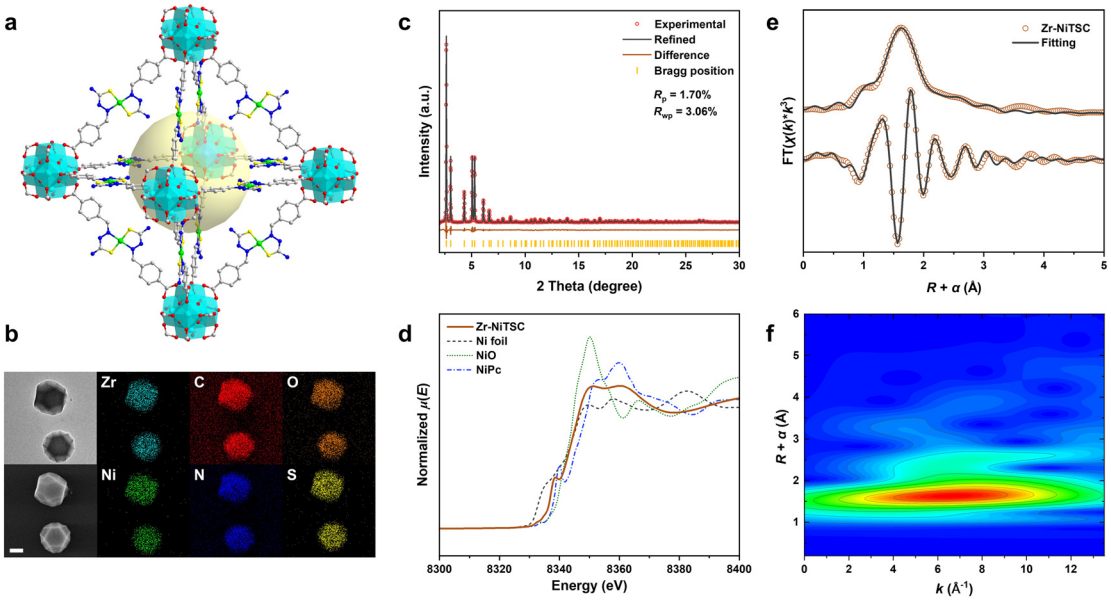

Fig. 2 (a) Structure diagram of Zr-NiTSC. (b) TEM image, STEM image, and elemental mapping of Zr-NiTSC. Scale bar of 200 nm. (c) Pawley refinement of Zr-NiTSC (synchrotron PXRD, λ = 0.98 Å). (d) Ni K-edge XANES spectra of Zr-NiTSC and standard samples Ni foil, NiO, and NiPc. (e) Ni K-edge EXAFS and the curvefit for Zr-NiTSC, shown in *R*-space (FT magnitude and imaginary component). (f) Wavelet transform of $\chi(k)$ of Zr-NiTSC.

Pawley refinement against synchrotron PXRD data (Fig. 2c and Table S2†). Notably, although isoreticular **fcu** MOFs with linkers of comparable length typically adopt interpenetrated architectures *via* direct synthesis,[29–31] PXRD analysis confirms that Zr-NiTSC has a non-interpenetrated framework. This deviation likely stems from the steric effect of the NiTSC moiety to prevent interpenetration. In addition, the low synthetic temperature (75 °C) may also favor the non-interpenetrated structure during one-pot assembly.

X-ray absorption fine structure (XAFS) spectroscopy was employed to further validate the structure of Zr-NiTSC. The Ni K-edge X-ray absorption near edge structure (XANES) spectrum confirms the +2 oxidation state of nickel (Fig. 2d), with a small pre-edge peak at 8332 eV attributed to the 1s → 3d transition that is similar to NiO and NiPc (Pc = phthalocyanine).[32,33] Notably, the peak observed at 8339 eV (similar to NiPc) originates from the 1s → $4p_z$ transition, characteristic of square–planar Ni(II) complexes with significant ligand-to-metal charge transfer (LMCT), which supports the structure of the planar Ni–N_2S_2 coordination center.[34–36] Extended X-ray absorption fine structure (EXAFS) fitting of Zr-NiTSC, using the Ni–N_2S_2 coordination geometry derived from the linker's single-crystal structure as the model, yielded excellent agreement (Fig. 2e). The main peak at 1.6 Å in the EXAFS spectra corresponds to the Ni–N and Ni–S bonds of the first coordination sphere, and each of the coordination number is 2. The peaks between 2 and 3 Å in the EXAFS spectra are attributed to the scattering of Ni with the C and N atoms adjacent to the coordinating N and S atoms in the TSC fragment (Fig. S7†). The absence of Ni–Ni scattering peaks in the wavelet transform (WT) plots (Fig. 2f) demonstrates the atomic-level dispersion of the Ni–N_2S_2 sites within the framework. These results strongly confirm that the NiTSC linker retains its designed square–planar Ni–N_2S_2 coordination within the framework.

Transmission electron microscopy (TEM) of Zr-NiTSC revealed well-defined microcrystals exhibiting a characteristic truncated octahedral morphology with sizes of ~400 nm (Fig. 2b and S8†). This morphology matches that of the Zr-MOFs with an **fcu** topology, such as the UiO-series and PCN-160,[37] consistent with our proposed structural model. Furthermore, energy-dispersive X-ray spectroscopy (EDS) mapping in scanning transmission electron microscopy mode confirmed the homogeneous spatial distribution of all the elements, especially Ni, N, and S, throughout the nanocrystals (Fig. 2b), confirming the successful synthesis of a compositionally uniform Zr-NiTSC framework. Thermogravimetric analysis (TGA) of Zr-NiTSC revealed a stepwise mass loss profile (Fig. S9†). The initial weight loss corresponds to desorption of physisorbed solvents from pores and the release of coordinated solvents bound to Zr or Ni sites. The decomposition of organic linkers begins at around 300 °C, with complete framework collapse occurring near 450 °C.

3.3 Introduction of photosensitizers into the Zr-NiTSC framework

The post-synthetic linker exchange was adopted to introduce photosensitizing DCPP linkers into the Zr-NiTSC framework. The NiTSC (18.4 Å) and DCPP (19.8 Å) exhibit comparable lengths (Fig. S5,† <8% length mismatch), ensuring successful linker exchange. We therefore incorporated DCPP photosensitizers into Zr-NiTSC *via* ligand exchange to enable subsequent photocatalytic reactions. The exchange reaction was

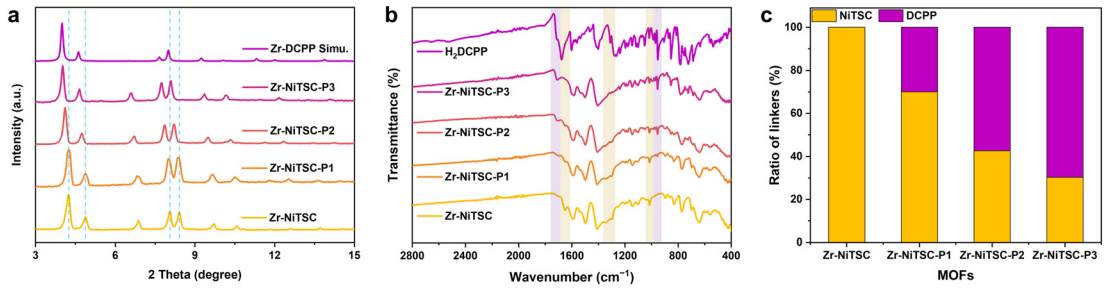

Fig. 3 (a) PXRD patterns of Zr-NiTSC, Zr-NiTSC-P1, P2, and P3, and simulated non-interpenetrated Zr-DCPP, with blue vertical lines marking the low-angle shifting of diffraction peaks. (b) FT-IR spectra of Zr-NiTSC, Zr-NiTSC-P1, P2, and P3, and H_2DCPP, with purple regions marking the increasing DCPP linkers and yellow regions marking the decreasing NiTSC linkers. (c) Ratio of NiTSC and DCPP linkers in Zr-NiTSC and Zr-NiTSC-P1, P2, and P3.

conducted by dispersing Zr-NiTSC and different concentrations of H_2DCPP in DMF at 75 °C. By varying the amount of H_2DCPP, we successfully obtained Zr-NiTSC-P1, P2, and P3. Notably, the color change from yellowish brown to deep magenta (Fig. S10†) is observed with an increasing porphyrin content, directly manifesting the progressive DCPP exchange.

To further confirm the successful DCPP incorporation, we conducted PXRD, TEM, Fourier transform infrared (FT-IR), and TGA characterization. PXRD patterns (Fig. 3a) reveal progressive low-angle shifting of diffraction peaks with increasing DCPP loading, indicating unit cell expansion due to the longer DCPP linker (19.8 Å *vs.* NiTSC: 18.4 Å).[38,39] The peak positions of Zr-NiTSC-P1, P2, and P3 lie in between those of pristine Zr-NiTSC and Zr-DCPP. The absence of peak splitting confirms a homogeneous mixed-linker MOF rather than phase-segregated Zr-NiTSC and Zr-DCPP mixtures. TEM imaging of Zr-NiTSC-P2 as a representative example confirms the preserved truncated octahedral morphology after linker exchange, and the EDS elemental mapping demonstrates homogeneous distribution of all elements throughout the crystal, collectively verifying that post-synthetic modification proceeds without framework degradation (Fig. S11†). FT-IR analysis further corroborates the progressive incorporation of DCPP linkers, revealing an inverse correlation between the characteristic bands of NiTSC and DCPP (Fig. 3b). Specifically, the spectra demonstrate a systematic enhancement of DCPP signatures, most notably the distinct N–H bending vibration in the porphyrin cores at 970 cm^{-1} diagnostic of metal-free porphyrin macrocycles, confirming the preservation of free-base porphyrin cores throughout the exchange process. Meanwhile, a concomitant attenuation of NiTSC vibrational modes was also observed, particularly manifested in the progressive weakening of the Ni–N stretching vibration at 1008 cm^{-1} as a direct indicator of decreasing NiTSC linkers. Furthermore, TGA curves revealed progressively diminishing residual masses for Zr-NiTSC-P1, Zr-NiTSC-P2, and Zr-NiTSC-P3, which also corroborates increased porphyrin incorporation within the framework (Fig. S12†). These relationships unambiguously confirm that the extent of ligand exchange scales directly with the initial H_2-DCPP dosage.

The DCPP content within the Zr-NiTSC-P*x* series was quantified *via* ultraviolet–visible (UV-vis) absorption spectroscopy. Precisely weighed samples of Zr-NiTSC-P*x* were digested with concentrated H_2SO_4, dissolved in DMSO, and diluted to appropriate concentrations. The concentrations were determined using a standard calibration curve of H_2DCPP in DMSO (Fig. S13, Table S3†), enabling the calculation of the NiTSC-to-DCPP molar ratios (Fig. S14, Table S4†). The results establish the simplified formulas of Zr-NiTSC-P1, P2, and P3 as $[Zr_6O_8][NiTSC]_{4.20}[DCPP]_{1.80}$, $[Zr_6O_8][NiTSC]_{2.56}[DCPP]_{3.44}$, and $[Zr_6O_8][NiTSC]_{1.82}[DCPP]_{4.18}$, respectively. The corresponding ligand molar ratios are visualized in Fig. 3c. Besides, the UV-vis spectrum of the digested Zr-NiTSC-P3 sample matched with that of free H_2DCPP (Fig. S15†), further excluding the formation of nickel porphyrin complexes within the framework.

3.4 Photophysical properties and photocatalytic performance

With the successful synthesis of Zr-NiTSC featuring Ni–N_2S_2 catalytic sites and the dual-functional Zr-NiTSC-P*x* series integrating both catalytic centers and porphyrin photosensitizers, we systematically investigated their photophysical properties and photocatalytic capabilities. The band structures of the parent and porphyrin-doped Zr-NiTSC were investigated using ultraviolet-visible-near infrared (UV-vis-NIR) diffuse reflectance spectroscopy (DRS) and Mott–Schottky analysis (Fig. S16 and S17†). The solid-state UV-vis-NIR spectra show that all porphyrin-doped materials (Zr-NiTSC-P1, P2, and P3) exhibit enhanced absorption in the visible region compared with undoped Zr-NiTSC (Fig. 4a), indicating improved light-harvesting capability. The estimated conduction band minimum (CBM) of all the samples remain above the H^+/H_2 redox potential (0 V *vs.* NHE), confirming the thermodynamic feasibility of proton reduction (Fig. 4b). Notably, porphyrin incorporation leads to an upward shift in the valence band maximum (VBM), resulting in a narrowed band gap. This trend suggests that porphyrin doping primarily affects the VBM, consistent with a higher HOMO of the porphyrin ligand.

To further investigate the impact of porphyrin incorporation on charge separation and photocatalytic performance, the transient photocurrent response and photocatalytic hydrogen

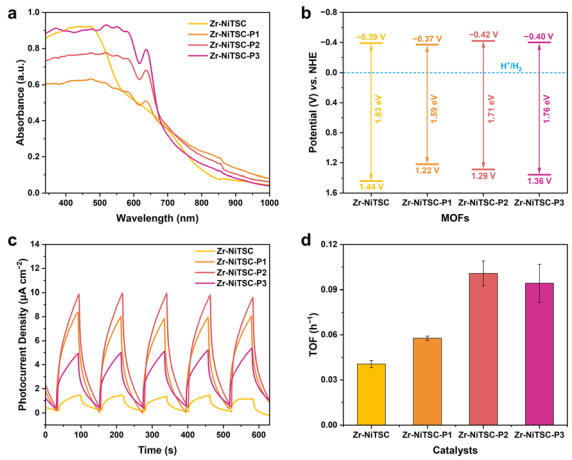

Fig. 4 (a) Normalized UV-vis-NIR DRS spectra of Zr-NiTSC and Zr-NiTSC-P1, P2, and P3. (b) Band structure of Zr-NiTSC and Zr-NiTSC-P1, P2, and P3. (c) Transient photocurrent response of Zr-NiTSC and Zr-NiTSC-P1, P2, and P3. (d) TOFs of the Ni–N_2S_2-based photocatalysts.

evolution reaction (HER) were conducted. All the porphyrin-doped samples exhibit higher photocurrent densities than the undoped Zr-NiTSC, indicating more efficient photoinduced charge separation (Fig. 4c). In the photocatalytic HER experiments (Fig. S18 and S19†), Zr-NiTSC, Zr-NiTSC-P1, and Zr-NiTSC-P2 exhibited progressively increasing H_2 production rates. However, Zr-NiTSC-P3 showed lower activity than the pristine Zr-NiTSC. Since porphyrin incorporation reduces the NiTSC density, we calculated turnover frequencies (TOFs) per Ni–N_2S_2 site to evaluate the intrinsic catalytic activity (Fig. 4d). Among the four MOFs, Zr-NiTSC-P2 displays the highest photocurrent, which correlates well with its maximum TOF of 0.10 h^{-1}. This strong agreement highlights the key role of charge separation in governing photocatalytic activity. In contrast, the decrease in both the photocurrent and TOF observed for Zr-NiTSC-P3 suggests that excessive porphyrin loading may introduce recombination centers and disrupt charge transport to the catalytic center. The non-monotonic activity trend underlines the necessity for precise control of the photosensitizer-to-catalyst molar ratio in dual-functional MOFs. While optimal photosensitizer incorporation augments the intrinsic activity of catalytic sites, excessive loading imposes kinetic constraints that ultimately diminish overall efficiency. Additionally, post-catalysis characterization of Zr-NiTSC-P2 confirmed the retention of framework integrity throughout the photocatalytic process, with PXRD revealing well-defined diffraction peaks (Fig. S20†) and TEM images (including STEM and EDS elemental mapping) showing a preserved truncated octahedral morphology and homogeneous elemental distribution (Fig. S21†).

4. Conclusions

In conclusion, we have developed a stepwise synthetic strategy for constructing biomimetic dual-functional MOF photocatalysts, which successfully integrates Ni–N_2S_2 catalytic centers and porphyrin photosensitizers within a stable Zr_6-based framework. Unlike traditional one-pot syntheses that fail to accommodate Ni–N_2S_2 sites under harsh solvothermal conditions, our approach first assembles the Zr-NiTSC framework under mild conditions and subsequently incorporates photosensitizing DCPP linkers through controlled post-synthetic linker exchange. This strategy allows precise control over the photosensitizer-to-catalyst ratio in mixed-linker Zr-NiTSC-P*x* to achieve optimized photocatalytic performance. Among the four MOFs, photocatalytic hydrogen evolution experiments exhibited a maximum at Zr-NiTSC-P2 (DCPP/NiTSC ≈ 1.3 : 1), delivering a 2.5-fold TOF enhancement over the parent framework, Zr-NiTSC, with deviations to higher or lower DCPP/NiTSC ratios reducing performance. These findings underscore that optimal photosensitizer/catalyst stoichiometry is paramount for photocatalytic efficiency. In addition to providing a generalizable synthetic strategy for integrating labile catalytic motifs and photosensitizers into a stable crystalline framework, this work provides a versatile platform for the design of synergistic catalysts for photocatalysis and broader energy conversion applications.

Data availability

Crystallographic data for the compounds have been deposited at the Cambridge Crystallographic Data Centre (CCDC) with the accession number 2419402, which can be accessed at **https://www.ccdc.cam.ac.uk/**. Materials, instrumentation details, synthesis procedures, and additional data including the crystallographic table, PXRD, EXAFS, TEM, TGA, UV-vis, photophysical measurements and photocatalysis are provided in the ESI† accompanying this article. This information is accessible at **https://doi.org/10.1039/D5CE00634A**.

Author contributions

S. Y. conceived the idea and supervised the research. Y. G. and X. X. performed the synthesis, most characterization and photocatalytic experiments. C. Z. and Y. G. analyzed the XAFS data. R. L. and Y. G. performed the TEM and FT-IR tests. S. Y., Y. G., and X. X. discussed the experimental data and wrote the paper. All the authors have approved the final version of the manuscript.

Conflicts of interest

There are no conflicts to declare.

Acknowledgements

This work was financially supported by the National Key Research and Development Program of China (2024YFA1510301), the National Natural Science Foundation of China (No. 22271141), the Fundamental Research Funds for the Central Universities (2024300376), Postdoctoral Fellowship Program of CPSF (GZB20240303), the China Postdoctoral Science Foundation (2024M751374), and Jiangsu Funding Program for Excellent Postdoctoral Talent (2024ZB547). We thank the staff of the BL17B

(https://cstr.cn/31129.02.NFPS.BL17B) and BL18U1 (https://cstr.cn/31129.02.NFPS.BL18U1) beamlines at the National Facility for Protein Science in Shanghai (NFPS, https://cstr.cn/31129.02.NFPS), Shanghai Advanced Research Institute, Chinese Academy of Sciences, for their technical support in data collection and analysis of XAFS and PXRD, respectively.

References

1 H. Li, Y. Nakajima, E. Nango, S. Owada, D. Yamada, K. Hashimoto, F. Luo, R. Tanaka, F. Akita, K. Kato, J. Kang, Y. Saitoh, S. Kishi, H. Yu, N. Matsubara, H. Fujii, M. Sugahara, M. Suzuki, T. Masuda, T. Kimura, T. N. Thao, S. Yonekura, L.-J. Yu, T. Tosha, K. Tono, Y. Joti, T. Hatsui, M. Yabashi, M. Kubo, S. Iwata, H. Isobe, K. Yamaguchi, M. Suga and J.-R. Shen, *Nature*, 2024, **626**, 670–677.
2 S. Xu, Y. Liu, B. Zhang, S. Li, X. Ye and Z.-G. Wang, *Acc. Mater. Res.*, 2024, **5**, 1072–1086.
3 H.-C. Zhou, J. R. Long and O. M. Yaghi, *Chem. Rev.*, 2012, **112**, 673–674.
4 H. Deng, C. J. Doonan, H. Furukawa, R. B. Ferreira, J. Towne, C. B. Knobler, B. Wang and O. M. Yaghi, *Science*, 2010, **327**, 846–850.
5 D. Kim, D. R. Whang and S. Y. Park, *J. Am. Chem. Soc.*, 2016, **138**, 8698–8701.
6 Y. Yin, S. Feng, X. Xu, Y. Liu, Y. Li, L. Gao, X. Zhou, J. Dong, Y. Wu, J. Su, J.-L. Zuo, S. Yuan and J. Zhu, *J. Am. Chem. Soc.*, 2025, **147**, 16481–16493.
7 G. Schulte, X.-L. Luo, R. H. Crabtree and M. Zimmer, *Angew. Chem., Int. Ed. Engl.*, 1991, **30**, 193–194.
8 M. Paudel, S. Karki, N. Acharya, S. Chapagain, J. V. Hemmer, D. T. Hofsommer, G. Gupta, R. M. Buchanan and C. A. Grapperhaus, *Dalton Trans.*, 2025, **54**, 5136–5142.
9 M. Paudel, S. Karki, K. Bajaj, D. T. Hofsommer, S. Parmar, M. S. Mashuta, P. M. Kozlowski, G. Gupta, R. M. Buchanan and C. A. Grapperhaus, *Inorg. Chim. Acta*, 2024, **572**, 122254.
10 X. Jing, Y. Yang, C. He, Z. Chang, J. N. H. Reek and C. Duan, *Angew. Chem., Int. Ed.*, 2017, **56**, 11759–11763.
11 G. Yang, D. Wang, Y. Wang, W. Hu, S. Hu, J. Jiang, J. Huang and H.-L. Jiang, *J. Am. Chem. Soc.*, 2024, **146**, 10798–10805.
12 Y. Li, J. Su, Y. Zhao, L. Feng, L. Gao, X. Xu, Y. Yin, Y. Liu, P. Xiao, L. Yuan, J.-S. Qin, Y. Wang, S. Yuan, H. Zheng and J.-L. Zuo, *J. Am. Chem. Soc.*, 2023, **145**, 10227–10235.
13 X. Xu, L. Gao and S. Yuan, *Dalton Trans.*, 2023, **52**, 15233–15252.
14 X.-J. Kong, T. He, J. Zhou, C. Zhao, T.-C. Li, X.-Q. Wu, K. Wang and J.-R. Li, *Small*, 2021, **17**, 2005357.
15 T. Jednačak, I. Mikulandra, K. Smokrović, A. Hloušek-Kasun, M. Kapustić, K. Delaš, I. Piantanida, M. Jurković, B. Bertoša, K. Zangger and P. Novak, *Bioorg. Chem.*, 2024, **147**, 107338.
16 S. M. Marschner, R. Haldar, O. Fuhr, C. Wöll and S. Bräse, *Chem. – Eur. J.*, 2021, **27**, 1390–1401.
17 A. D. Burrows, R. W. Harrington, M. F. Mahon and S. J. Teat, *CrystEngComm*, 2002, **4**, 539–544.
18 A. D. Burrows, R. W. Harrington, M. F. Mahon and S. J. Teat, *Cryst. Growth Des.*, 2004, **4**, 813–822.
19 N. T. Akinchan, R. Akinchan, U. J. Ibok, L. P. Battaglia, A. Bonamartini Corradi and P. Drożdżewski, *J. Crystallogr. Spectrosc. Res.*, 1992, **22**, 741–753.
20 U. M. Osman, S. Silvarajoo, M. F. Noor Hassim, S. Arshad, A. H. Anizaim and F. I. Abdul Razak, *Bioinorg. Chem. Appl.*, 2021, **2021**, 5536902.
21 F. Bisceglie, S. Pinelli, R. Alinovi, M. Goldoni, A. Mutti, A. Camerini, L. Piola, P. Tarasconi and G. Pelosi, *J. Inorg. Biochem.*, 2014, **140**, 111–125.
22 P. S. Zhao, H. Y. Wang, J. Song and L. D. Lu, *Struct. Chem.*, 2010, **21**, 977–987.
23 J. K. Bilyj, M. J. Riley and P. V. Bernhardt, *Dalton Trans.*, 2018, **47**, 2018–2030.
24 M. N. Donohoe, A. Upadhyay and D. A. Pratt, *J. Am. Chem. Soc.*, 2024, **146**, 31307–31320.
25 C. González-García, M. A. Mendiola, J. Perles and E. López-Torres, *CrystEngComm*, 2017, **19**, 1035–1044.
26 S. Yuan, L. Feng, K. Wang, J. Pang, M. Bosch, C. Lollar, Y. Sun, J. Qin, X. Yang, P. Zhang, Q. Wang, L. Zou, Y. Zhang, L. Zhang, Y. Fang, J. Li and H.-C. Zhou, *Adv. Mater.*, 2018, **30**, 1704303.
27 P. F. Muldoon, C. Liu, C. C. Miller, S. B. Koby, A. Gamble Jarvi, T.-Y. Luo, S. Saxena, M. O'Keeffe and N. L. Rosi, *J. Am. Chem. Soc.*, 2018, **140**, 6194–6198.
28 J. Winarta, B. Shan, S. M. McIntyre, L. Ye, C. Wang, J. Liu and B. Mu, *Cryst. Growth Des.*, 2020, **20**, 1347–1362.
29 J. Lyu, X. Zhang, Z. Chen, R. Anderson, X. Wang, M. C. Wasson, P. Bai, X. Guo, T. Islamoglu, D. A. Gómez-Gualdrón and O. K. Farha, *ACS Appl. Mater. Interfaces*, 2019, **11**, 42179–42185.
30 U. S. F. Arrozi, V. Bon, S. Krause, T. Lübken, M. S. Weiss, I. Senkovska and S. Kaskel, *Inorg. Chem.*, 2020, **59**, 350–359.
31 L. Feng, S. Yuan, J.-S. Qin, Y. Wang, A. Kirchon, D. Qiu, L. Cheng, S. T. Madrahimov and H.-C. Zhou, *Matter*, 2019, **1**, 156–167.
32 A. Anspoks and A. Kuzmin, *J. Non-Cryst. Solids*, 2011, **357**, 2604–2610.
33 P. Acharya, J. Hong, R. Manso, A. S. Hoffman, L. Kekedy-Nagy, J. Chen, S. R. Bare and L. F. Greenlee, *J. Phys. Chem. C*, 2023, **127**, 11891–11901.
34 X. Wang, Y. Fu, D. Tranca, K. Jiang, J. Zhu, J. Zhang, S. Han, C. Ke, C. Lu and X. Zhuang, *ACS Appl. Energy Mater.*, 2021, **4**, 2891–2898.
35 X. Ottenwaelder, A. Aukauloo, Y. Journaux, R. Carrasco, J. Cano, B. Cervera, I. Castro, S. Curreli, M. C. Muñoz, A. L. Roselló, B. Soto and R. Ruiz-García, *Dalton Trans.*, 2005, 2516–2526.
36 L. R. Furenlid, M. W. Renner and E. Fujita, *Phys. B*, 1995, **208–209**, 739–742.
37 S. Yuan, L. Zou, J.-S. Qin, J. Li, L. Huang, L. Feng, X. Wang, M. Bosch, A. Alsalme, T. Cagin and H.-C. Zhou, *Nat. Commun.*, 2017, **8**, 15356.
38 S. Yuan, L. Huang, Z. Huang, D. Sun, J.-S. Qin, L. Feng, J. Li, X. Zou, T. Cagin and H.-C. Zhou, *J. Am. Chem. Soc.*, 2020, **142**, 4732–4738.
39 Y.-X. Gao, X.-N. Yi, Z.-C. Tang, H. Yang, W. Wang, M. Xu and Z.-Y. Gu, *Anal. Chem.*, 2024, **96**, 6476–6482.